

# Geochemistry, zircon U–Pb geochronology, and Hf isotope of the late Permian Sa Thay granite from Kontum massif: Petrogenesis and tectonic implications

PHAM Minh<sup>1,2,\*</sup>, NGUYEN Huu Trong<sup>3,4,\*</sup>, PHAM Trung Hieu<sup>1,2</sup>

<sup>1</sup> Faculty of Geology, University of Science, Ho Chi Minh City, 227 Nguyen Van Cu Str, 5 district, Ho Chi Minh City, Viet Nam

<sup>2</sup> Vietnam National University Ho Chi Minh City, Thu Duc city, Ho Chi Minh city, Vietnam

<sup>3</sup> Faculty of Geosciences and Geoengineering, Hanoi University of Mining and Geology, 18 Pho Vien Str, Duc Thang, Bac Tu Liem, Hanoi, Vietnam

<sup>4</sup> HiTech-CEAE Research Team, Hanoi University of Mining and Geology, 18 Pho Vien Str, Duc Thang, Bac Tu Liem, Hanoi, Vietnam

\* Corresponding email: [pminh@hcmus.edu.vn](mailto:pminh@hcmus.edu.vn); [nguyenhutrong@hmg.edu.vn](mailto:nguyenhutrong@hmg.edu.vn)

**Abstract:** Sa Thay high-K granites, situated in the western region of Kontum massif, are predominantly composed of biotite granite and biotite-hornblende granite. The major mineral composition comprises plagioclase (26–60%), K-feldspar (8–22%), quartz (15–33%), biotite (3–7%), and hornblende (7–10%). Accessory minerals include titanite, apatite, zircon, and magnetite. Their SiO<sub>2</sub> concentration varies from 66.81 to 78.14 wt.%, total alkali content ranges from 6.30 to 6.46 wt.%, and A/CNK ratio goes from 0.99 to 1.09. The granites indicate the relative enrichment of large-ion lithophile elements (Sc, Rb, and K), and the negative anomalies for Nb, Ta, and Ti in mantle-normalized diagrams. The P<sub>2</sub>O<sub>5</sub> content decreases with the increase of SiO<sub>2</sub> content, whilst there is a coupled increase in Th and Tb contents typical of I-type granites. The U–Pb zircon age was determined by the LA-ICP-MS method as 256.7 Ma, corresponding to the Late Permian stage. The  $\varepsilon_{\text{Hf}}(t)$  values, together with the zircon Hf model ages ( $T_{\text{DM}2}$ ) of 1440–1861 Ma, suggest that parental magma for the Sa Thay granite is derived from the partial melting of Paleoproterozoic mantle rocks and the input of crustal component, following the subduction-collision processes that resulted in the amalgamation of the South China and Indochina blocks (Indosinian Orogeny). This geological activity led to the closure of a branch of the Paleo-Tethys Ocean along the Song Ma suture zone during the Late Permian to Early Triassic period.

**Keywords:** Sa Thay granite; Indosinian Orogeny; Permian-Triassic; Hf isotope; I-type granite

## 1. Introduction

Granitoids are relatively abundant in the Sa Thay district of Kon Tum province which spreads across the area of approximately 75 km<sup>2</sup>. On the geological map of Vietnam 1:200,000 [1], specifically, the Sa Thay granite outcrops, as well as the intrusive rocks in the western area of Kontum massif, are described as the Dien Binh complex with Silurian age ( $\gamma\delta\text{Sdb}_2$ ).

Subsequently, when the Kon Tum-Buon Me Thuot sheet group's geology was measured and mapped at a scale of 1:50,000 [2], these granites were later categorized as part of the Dinh Quan Complex ( $K\bar{d}q_1$ ). These ages are primarily determined by the rock composition and the geological relationships between the granitoid masses and surrounding formations. Vu (2014) concluded that the Sa Thay granite rocks established about 240.5 Ma based on the LA-ICP-MS U–Pb zircon age. Additionally, in the studied region the granite formations in the Sa Thay area are spatially associated with andesitic rocks dating to 265.5 Ma [3]. In addition, the study area contains a variety of minerals associated with the Sa Thay granites, including Cu, Au, and Mo porphyry [4] and gold ore deposits spreading west of the Poko suture zone. They are part of the gold-quartz system, gold-quartz-sulfur system, gold-quartz-sulfur-polymetallic system, and gold-sulfur-polymetallic system [1, 2, 4]. Thus, the formation age and origin of the Sa Thay granite remain consistent with the current understanding. To better understand the evolutionary history of the Kon Tum massif, we investigate the geochemistry, zircon U–Pb dating, and Hf isotopic analysis to elucidate the material composition, origin, and formation setting of the Sa Thay granite.

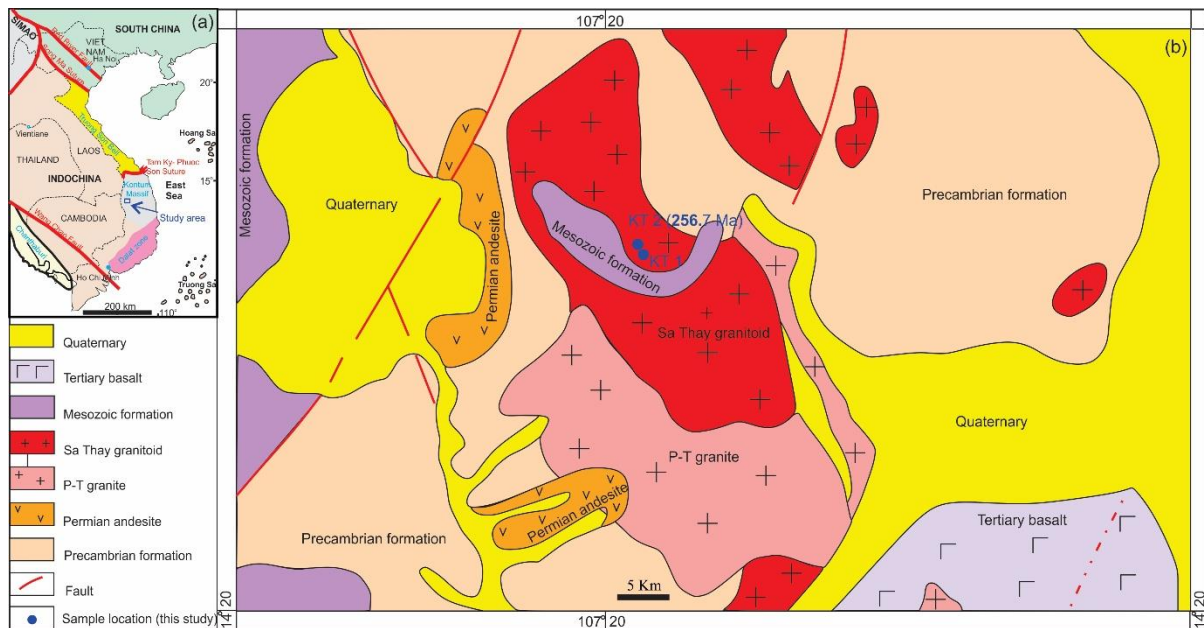


**Fig. 1.** (a) Geological tectonic frame of Southeast Asia, indicating three main structural zones within the Indochina block [5]. (b) Schematic map showing the Kontum geological and lithological features [1].

## 2. Geological setting and sample location

### 2.1. Geological setting

The Kontum massif is part of the Indochina block, which borders the Dalat zone to the south and the Truong Son orogenic belt to the north, with boundaries defined by the Tam Ky-Phuoc Son suture zone and the Poko River suture zone (Fig. 1a). The lithology of the Kontum massif is mostly composed of metamorphic rocks with high-grade amphibolite to granulite facies and mafic to felsic magmatic rocks [5]. Recent studies on the thermodynamic processes and regional tectonic evolution of the Kontum massif and neighboring areas [6-10] indicate that this region has undergone a polyphase metamorphic process. Quantitative analyses of granitoids in the area reveal two primary stages of formation: the Ordovician-Silurian [11-15] and the Permian-Triassic [3, 16-18]. The research region (Fig. 1b) primarily contains the Precambrian metamorphic, the Permian-Triassic plutonic, and volcanic rocks. Additionally, the Cenozoic basalt and the Quaternary deposits are also present.

### 2.2. Sample location and lithological characteristics

The granites were taken from the Cuu Long stone quarry, located about 20 km from Sa Thay town, with geographical coordinates (14°23'9.830"N; 107°50'56.978"E). The samples include biotite-hornblende granite and a smaller proportion of biotite granite (Fig. 2a), which are gray-white with black spots, exhibiting a massive structure, oscillatory zoning texture, and subhedral crystal shape. The block also contains black, fine-grained dioritic xenoliths that are oval or spherical in shape (Fig. 2b), ranging in size from 10 cm to 20 cm. The mineral composition of the Sa Thay granite comprises plagioclase (40–60%), K-feldspar (25–38%), quartz (15–20), biotite (5–10%), and hornblende (5–10%) (Fig. 2c, d). Accessory minerals include apatite, titanite, zircon, and magnetite. The dioritic xenoliths are predominantly composed of plagioclase (45–60%), hornblende (15–30%), biotite (10–20%), and quartz (5–10%). The fault system, trending in a latitudinal direction and northeast-southwest, cuts through the Sa Thay granite, causing fracturing and mylonitization. The crushed zone of this granite frequently contains high concentrations of sulfur, sericite, and chlorite.

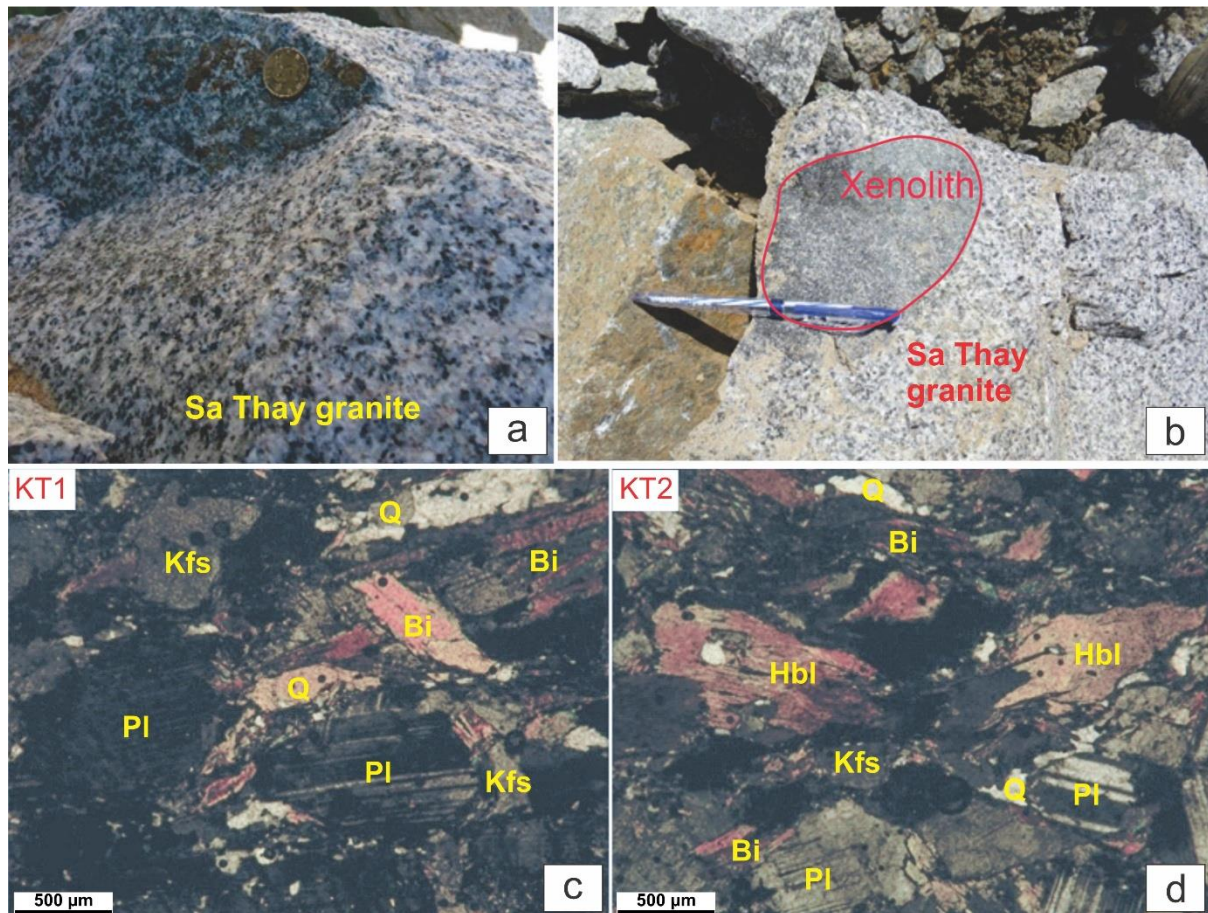


**Fig. 2.** (a, b) Representative field of the Sa Thay pluton and (c, d) photomicrographs of Sa Thay minerals. Mineral abbreviations: Pl: plagioclase, Kfs: K-feldspar, Qz: quartz, Bt: biotite and Hbl: Hornblende.

### 3. Applied methodologies

#### 3.1. Whole-rock geochemistry

A corundum jaw crusher was used to smash fresh rock samples to less than 5 mm. A vibratory disc mill (RS200, Retsch GmbH, Germany), equipped with a tungsten carbide milling cup, was utilized to grind a sample weighing around 100 g to less than 200 mesh (~75 µm). Comprehensive major element analyses of bulk rock samples were performed utilizing X-ray fluorescence (XRF) technology (Primus II, Rigaku, Japan) at Wuhan Sample Solution Analytical Technology Co., Ltd (WSSATCL) in Wuhan, China. XRF technology determines the major element composition by measuring the characteristic fluorescence emitted by elements under X-ray irradiation. The analytical accuracy for all key elements has a relative error of less than 2%.

Approximately 50 mg of rock powder was subjected to digestion using a mixture of HF and HNO<sub>3</sub> within teflon vessels. The resultant solution was subsequently analyzed for trace elements utilizing inductively coupled plasma mass spectrometry (ICP-MS, Agilent 7700e) at WSSATCL in Wuhan, China. Liu (2008) provides a detailed description of the sample digestion process, including the analytical accuracy and precision of the trace elements.

#### 3.2. Zircon separation and cathodoluminescence imaging

Zircon grains were isolated employing conventional magnetic and density separation methodologies. Zircon crystals were meticulously selected under a stereoscopic microscope and subsequently embedded in epoxy resin prior to the polishing process. The cathodoluminescence images of the analyzed zircon grain were acquired at WSSATCL, utilizing a scanning electron microscope (JSM-IT100) linked to a Gatan MiniCL system. The imaging parameter was set at a voltage range of 10.0 to 13.0 kV, with a tungsten filament current of 80 to 85 µA.

#### 3.3. U-Pb dating and trace element analysis of zircon by LA-ICP-MS

Laser ablation inductively coupled plasma mass spectrometry (LA-ICP-MS) was used for both U-Pb dating and trace element analyses of zircon grains at the State Key Laboratory of Geological Processes and Mineral Resources, China University of Geosciences, Wuhan. Liu (2008), Liu (2010), Liu (2010) provide

specific operating settings for the ICP-MS equipment, laser ablation system, and data reduction process. Laser sampling was conducted using a Geolas 2005 excimer ArF laser ablation system manufactured by Lambda Physik in Göttingen, Germany. Ion signal intensities were measured using an Agilent 7500a ICP-MS instrument. Each analysis began with a preliminary background acquisition lasting approximately 20 to 30 seconds (gas blank), followed by a 50-second data acquisition period from the zircon. For U-Pb dating, zircon 91500 was used as an external reference. Time-dependent variations in U-Th-Pb isotopic ratios were corrected through linear interpolation over time for every five analyses, based on fluctuations observed in the 91500 zircon standard [21]. The preferred U-Th-Pb isotopic ratios for the sample 91500 standard were taken from reference [23]. With silicon serving as the internal element, the trace element compositions of zircon were calibrated. Data acquisition for each analysis was managed using Agilent ChemStation software. Offline selection, integration, time-drift correction, and quantitative calibration for U-Pb dating and trace element analysis were performed using ICPMSDataCal [20, 21]. Weighted mean calculations and Concordia diagrams were generated using Isoplot/Ex\_ver3 [24].

### 3.4. *In situ* Lu-Hf isotope

At the State Key Laboratory of Geological Processes and Mineral Resources, China University of Geosciences, Wuhan, *in situ* zircon Lu-Hf isotope was performed using a Neptune Plus MC-ICP-MS (Germany) coupled with a Geolas 2005 excimer ArF laser ablation system (Germany). This laser ablation system is equipped with a "wire" signal filtering device [25]. Helium served as the carrier gas within the ablation cell and was subsequently combined with argon, which functioned as the make-up gas. Prior research has indicated that a more uniform two-fold signal enhancement was attained through the utilization of helium in place of argon for the 193 nm laser [26]. A straightforward Y junction was employed downstream from the sample cell to introduce minimal quantities of nitrogen ( $4 \text{ ml min}^{-1}$ ) into the argon make-up gas flow [26]. In comparison to the conventional configuration, the incorporation of nitrogen, along with the utilization of a newly engineered X skimmer and Jet sample cones in the Neptune Plus, resulted in an enhancement of signal intensity for Hf, Yb, and Lu by factors of 5.3, 4.0, and 2.4, respectively. In the current investigation, all zircon data were obtained utilizing single spot ablation mode with a spot diameter of  $44 \mu\text{m}$ . Each measurement comprised a 20-second acquisition of the baseline signal, succeeded by a 50-second acquisition of the ablation signal. Comprehensive operating conditions for the laser ablation system, as well as the MC-ICP-MS instrument and its associated analytical methodology, are delineated in Hu (2012). The offline selection and integration of analyte signals, as well as the calibration for mass bias, were conducted utilizing ICP-MS DataCal [20, 21].

The measured  $^{176}\text{Lu}/^{177}\text{Hf}$  ratios and the  $^{176}\text{Lu}$  decay constant of  $1.867 \times 10^{-11} \text{ yr}^{-1}$  [28] were applied to calculate the initial  $^{176}\text{Hf}/^{177}\text{Hf}$  ratios. The chondritic values of  $^{176}\text{Lu}/^{177}\text{Hf} = 0.0332$  and  $^{176}\text{Hf}/^{177}\text{Hf} = 0.282772$  were used to get the  $\varepsilon_{\text{Hf}}$  values [29]. The model ages of the depleted mantle ( $T_{\text{DM}}$ ) were derived from the measured ratios of  $^{176}\text{Lu}/^{177}\text{Hf}$ , predicated on the assumption that the depleted mantle reservoir exhibits a linear isotopic evolution from an initial  $^{176}\text{Hf}/^{177}\text{Hf}$  ratio of 0.279718 at 4.55 Ga to a current ratio of 0.283250, with a  $^{176}\text{Lu}/^{177}\text{Hf}$  ratio of 0.0384 [30]. The two-stage model age ( $T_{\text{DM2}}$ ) was determined for each zircon sample, assuming that the parental magma was produced from the upper continent crust ( $^{176}\text{Lu}/^{177}\text{Hf} = 0.0093$ ) that was initially sourced from the depleted mantle [31].

## 4. Analytical results

### 4.1. Geochemistry

The detailed composition of major and trace elements in the Sa Thay granite is presented in Table 1. The  $\text{SiO}_2$  concentration varies significantly, ranging from 66.81 to 78.14 wt.%. The  $\text{Al}_2\text{O}_3$  content ranges from 11.31 to 14.78 wt.%, while the  $\text{Na}_2\text{O}$  content ranges between 2.81 and 2.84 wt.%,  $\text{K}_2\text{O}$  content ranges from 3.5 to 3.62 wt.%, with a high total alkali ( $\text{K}_2\text{O} + \text{Na}_2\text{O}$ ) of 6.30 to 6.46 wt.%, and a  $\text{K}_2\text{O}/\text{Na}_2\text{O}$  ratio between 1.25 and 1.27 (i.e., greater than 1). In the TAS diagram (Fig. 3a), the Sa Thay granites fall within the granodiorite and granite fields, as well as the medium and high potassium fields (Fig. 3b). The  $\text{CaO}$  concentration varies significantly, ranging from 0.97 to 3.58 wt.%. The contents of total iron oxide ( $\text{Fe}_2\text{O}_3^{\text{t}}$ ) and  $\text{MgO}$  are 1.45 to 4.41 wt.% and 0.44 to 1.87 wt.%, respectively. The Sa Thay granites exhibit an aluminum saturation index (A/CNK) below 1.1 for all samples, with values ranging from 0.99 to 1.09, classifying them as metaluminous (Fig. 3c). Based on the granite classification diagram of  $((\text{K}_2\text{O} + \text{Na}_2\text{O})/\text{CaO})$  vs.  $\text{Zr} + \text{Nb} + \text{Ce} + \text{Y}$  [32], the samples plot within the fields of I-type, S-type, and M-type granites (Fig. 3d). Additionally, in the  $\text{P}_2\text{O}_5$  vs.  $\text{SiO}_2$  and Y vs. Rb diagrams (Fig. 3e, f), all samples align with the trend typical of I-type granites.

**Tab. 1.** Major element content of the Sa Thay granite.

| Sample                                      | KT1             | KT2                        |
|---|-----------------|----------------------------|
| Litology                                    | Biotite granite | Biotite-hornblende granite |
| SiO <sub>2</sub>                            | 78.136          | 66.806                     |
| TiO <sub>2</sub>                            | 0.245           | 0.575                      |
| Al <sub>2</sub> O <sub>3</sub>              | 11.309          | 14.782                     |
| Fe <sub>2</sub> O <sub>3</sub> <sup>t</sup> | 1.453           | 4.41                       |
| MnO   | 0.055           | 0.069                      |
| MgO   | 0.436           | 1.867                      |
| CaO   | 0.974           | 3.579                      |
| Na <sub>2</sub> O                           | 2.842           | 2.807                      |
| K <sub>2</sub> O                            | 3.618           | 3.497                      |
| P <sub>2</sub> O <sub>5</sub>               | 0.069           | 0.14                       |
| LOI   | 1.30            | 1.81                       |
| A/CNK                                       | 1.090           | 0.990                      |
| A/NK  | 1.315           | 1.758                      |

A/CNK value: molar Al<sub>2</sub>O<sub>3</sub>/(CaO+Na<sub>2</sub>O+K<sub>2</sub>O) and A/NK value: molar Al<sub>2</sub>O<sub>3</sub>/(Na<sub>2</sub>O+K<sub>2</sub>O).

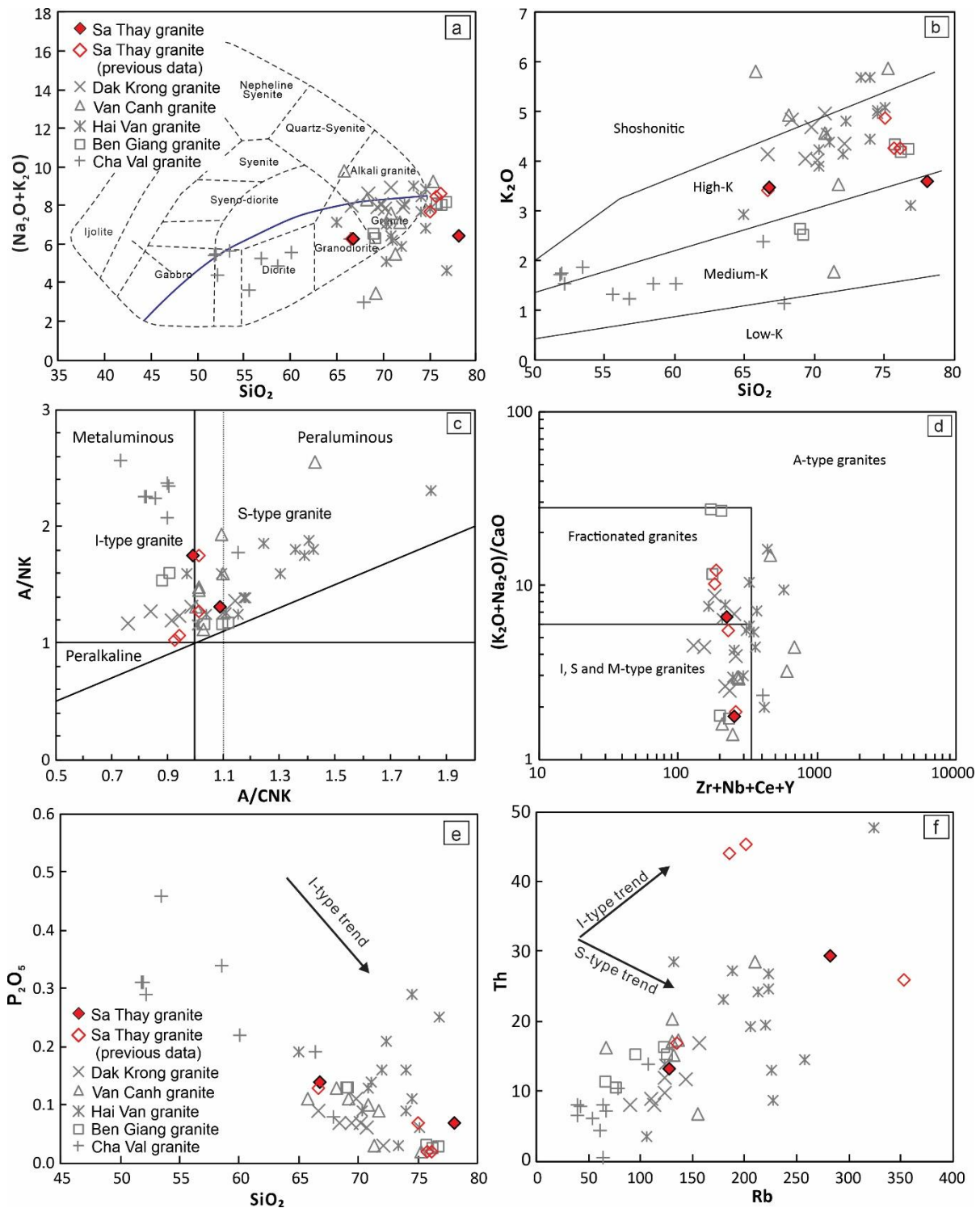


**Fig. 3.** (a) Total alkali ( $\text{Na}_2\text{O}+\text{K}_2\text{O}$ ) versus  $\text{SiO}_2$  diagram after Middlemost (1994), (b)  $\text{K}_2\text{O}$  versus  $\text{SiO}_2$  diagram of the granite based on the classification scheme of Peccerillo (1976), (c)  $\text{A}/\text{NK}$  versus  $\text{A}/\text{CNK}$  diagram proposed by Maniar (1989), (d)  $((\text{K}_2\text{O} + \text{Na}_2\text{O})/\text{CaO})$  versus  $\text{Zr}+\text{Nb}+\text{Ce}+\text{Y}$  [32], (e, f) The trend of I- and S-type granites [36]. Other data are cited from [37] (Sa Thay granite), [38] (Dak Krong granite), [39] (Hai Van granite, and Ben Giang granite), [40] (Hai Van granite), [16] (Cha Val granite).

The Sa Thay granites exhibit a notable abundance of rare earth elements (REE), with total REE concentrations ( $\sum\text{REE}$ ) ranging from 143.19 to 171.69 ppm. The ratio of light rare earth elements (LREE is La, Ce, Pr, Nd, Sm, and Eu) to heavy rare earth elements (HREE is Gd, Tb, Dy, Ho, Er, Tm, Yb, and Lu) ( $\text{LREE}/\text{HREE}$ ) varies between 7.72 and 10.02, while the normalized ratio of  $(\text{La}/\text{Y})_n$  ranges from 8.04 to 12.04. In the chondrite-normalized trace element patterns, the REE distribution exhibits a left-to-right inclination, reflecting a transition from REE to HREE. A significant negative Eu anomaly is observed, with values of  $\delta\text{Eu}$  ranging from 0.2 to 0.78. In the primitive mantle-normalized trace element patterns, the

samples are enriched in large ion radius lipophilic elements (LILE) such as Rb, Th, U, Ce, and Pb, but depleted in high field strength elements (HFSE) elements such as Ta, and Ti. The negative anomalies for Ba, Nb, Eu, and Sr are attributed to the crystallization and differentiation of plagioclase and K-feldspar (Fig. 4).

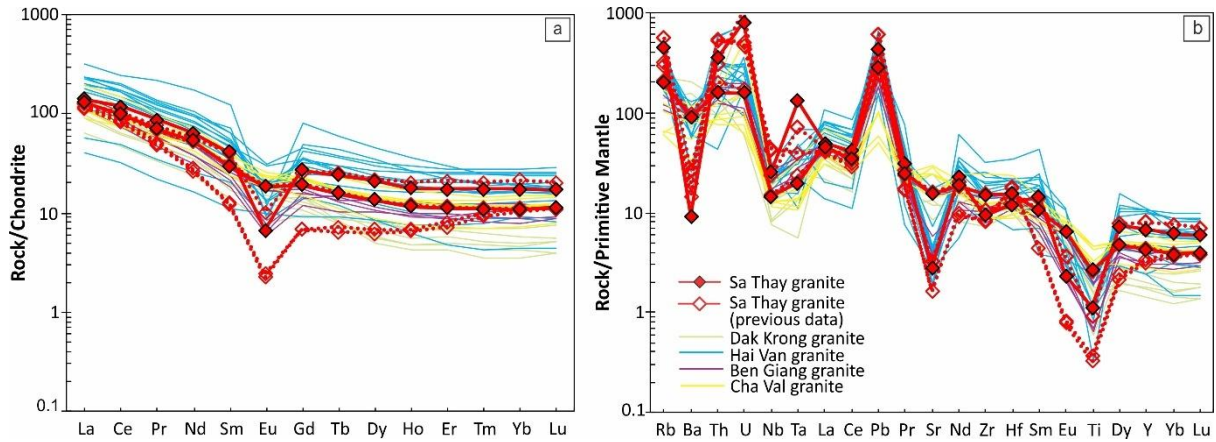


**Fig. 4.** Chondrite-normalized trace element concentrations (a) and Primitive-mantle normalized concentrations (b) of the Sa Thay granite from the Kontum massif. The normalized values are from Sun (1989). Additional data are referenced from [37] (Sa Thay granite), (Dak Krong granite), [39] (Hai Van granite, and Ben Giang granite), [40] (Hai Van granite), [16] (Cha Val granite).

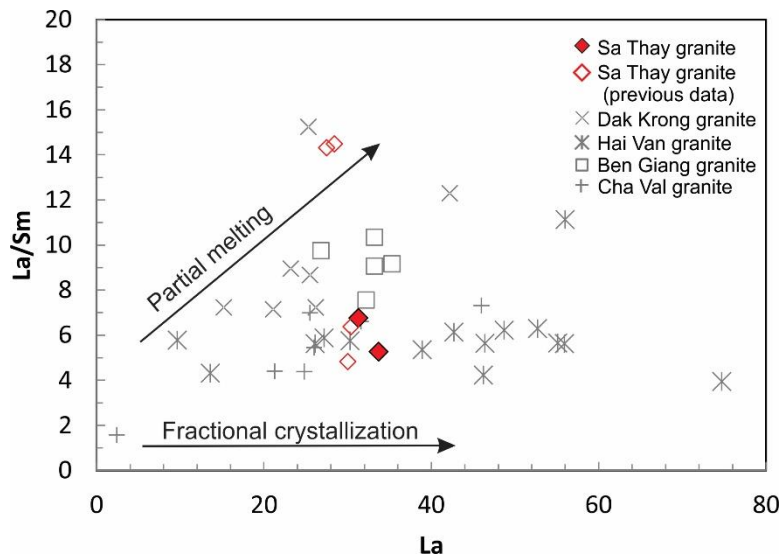


**Fig. 5.** La vs. La/Sm diagram for discrimination between fractional crystallization and partial melting trends [42]. Other data are cited from [37] (Sa Thay granite), [38] (Dak Krong granite), [39] (Hai Van granite, and Ben Giang granite), [40] (Hai Van granite), [16] (Cha Val granite).

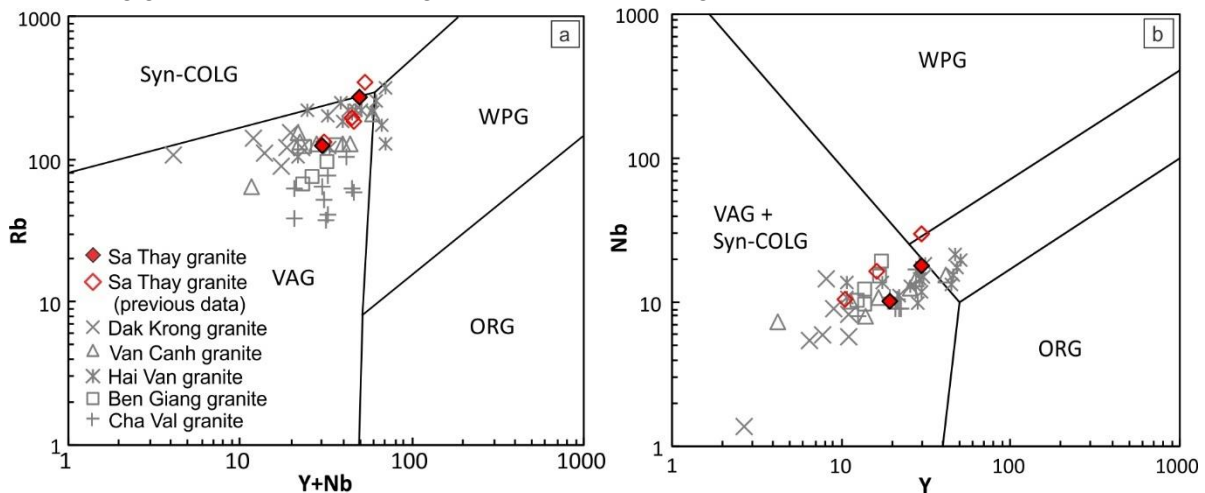


**Fig. 6.** (a, b) Geotectonic discrimination [43]. Other data are cited from [37] (Sa Thay granite), [38] (Dak Krong granite), [39] (Hai Van granite, and Ben Giang granite), [40] (Hai Van granite), [16] (Cha Val granite). VAG: volcanic arc granite, Syn-COLG: syn-collisional granite, WPG: within plate granite, and ORG: ocean ridge granite.

**Tab. 2.** Trace and rare earth element compositions of the Sa Thay granite.

| Sample | KT1    | KT2    | Sample               | KT1    | KT2    |
|--------|--------|--------|----------------------|--------|--------|
| Sc     | 4.50   | 10.40  | Sm                   | 6.39   | 4.62   |
| V      | 15.12  | 75.05  | Eu                   | 0.39   | 1.08   |
| Cr     | 2.49   | 41.63  | Gd                   | 5.57   | 3.94   |
| Co     | 91.93  | 38.10  | Tb                   | 0.90   | 0.60   |
| Ni     | 3.43   | 10.73  | Dy                   | 5.35   | 3.48   |
| Cu     | 2.54   | 4.22   | Ho                   | 1.01   | 0.66   |
| Zn     | 31.19  | 52.38  | Er                   | 2.92   | 1.89   |
| Ga     | 15.09  | 17.92  | Tm                   | 0.44   | 0.28   |
| Rb     | 281.29 | 126.47 | Yb                   | 3.00   | 1.86   |
| Sr     | 58.21  | 324.59 | Lu                   | 0.44   | 0.29   |
| Zr     | 103.84 | 167.07 | Y                    | 30.46  | 19.41  |
| Nb     | 18.20  | 10.32  | Li                   | 43.83  | 10.43  |
| Cs     | 12.57  | 2.12   | Be                   | 66.80  | 2.04   |
| Ba     | 63.84  | 636.73 | T° C                 | 762.75 | 780.39 |
| Hf     | 3.66   | 4.69   | 10000Ga/Al           | 2.52   | 2.29   |
| Ta     | 5.35   | 0.80   | Eu/Eu*               | 0.20   | 0.78   |
| Pb     | 30.47  | 20.17  | ∑LREE                | 152.04 | 130.20 |
| Th     | 29.55  | 13.27  | ∑HREE                | 19.64  | 13.00  |
| U      | 16.69  | 3.31   | ∑REE                 | 171.69 | 143.19 |
| La     | 33.68  | 31.27  | (La/Yb) <sub>n</sub> | 8.04   | 12.04  |
| Ce     | 73.04  | 61.09  | (Tb/Yb) <sub>n</sub> | 1.37   | 1.45   |
| Pr     | 8.36   | 6.82   | (La/Nd) <sub>n</sub> | 2.20   | 2.43   |
| Nd     | 30.19  | 25.31  | Nb/Ta                | 3.40   | 12.90  |

$$Eu/Eu^* = Eu_n / (Sm_n * Gd_n)^{1/2}$$

#### 4.2. Results of CL analysis and U-Pb zircon isotopic age

Cathodoluminescence (CL) images of representative zircon minerals from sample KT2 are shown in Fig. 7. The zircon grains in sample KT2 range in size from 80 to 150 μm. Under CL imaging, the zircon grains appear relatively bright in color and are generally rounded at the edges. Some grains exhibit unclear or absent internal zoning structures.

The results of the U-Pb isotope analysis of these zircons are presented in Table 3 and illustrated in Figure 8. Fourteen analysis points on 14 different zircon grains indicate a Th/U ratio ranging from 0.31 to 0.35, which is greater than 0.1, confirming that the zircons crystallized from a magmatic source [44, 45].

The measured  $^{206}\text{Pb}/^{238}\text{U}$  zircon isotopic ages for sample KT2 range from 244 Ma to 261 Ma, showing minimal variation over this interval.

The positive Pb anomaly suggests the involvement of Pb-enriched sources of subduction zone environments, where Pb is preferentially mobilized and introduced into the mantle wedge or ascending magmas [46, 47]. On the Concordia diagram (Fig. 8a, b), these ages cluster closely along the Concordia curve, yielding a weighted mean age of  $256.7 \pm 7.1$  Ma (MSWD = 2.6, n=14). This age represents the crystallization of the Sa Thay granites, placing their formation in the Late Permian-Early Triassic period.

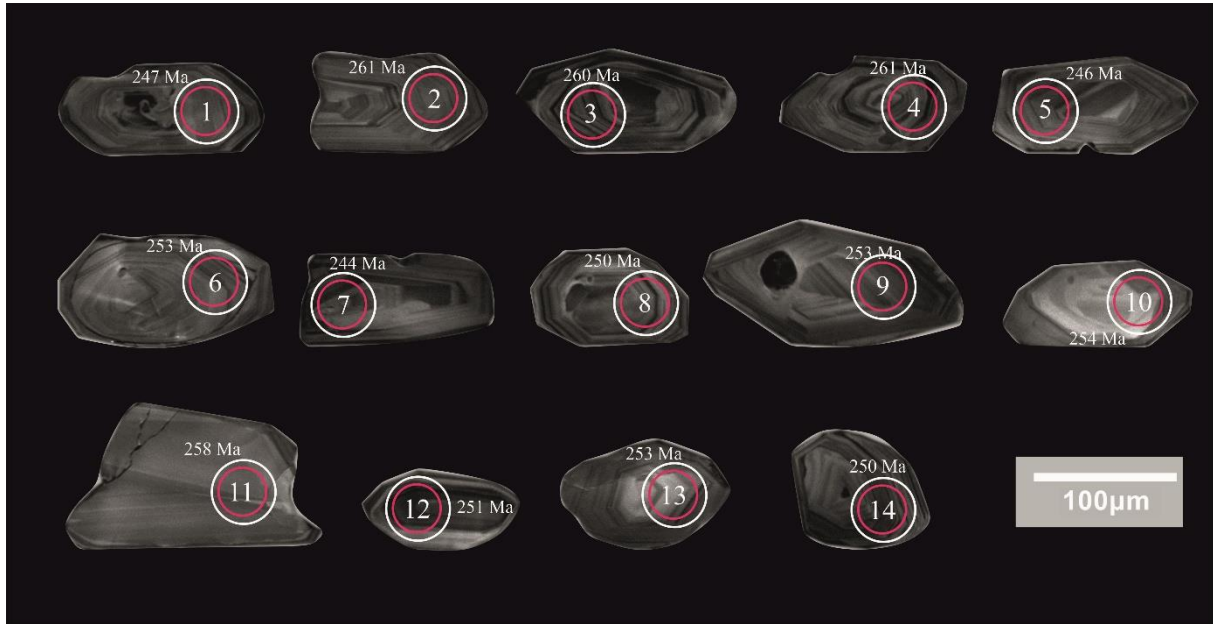


**Fig. 7.** Cathodoluminescence (CL) images of representative zircon grains from the Sa Thay granite.

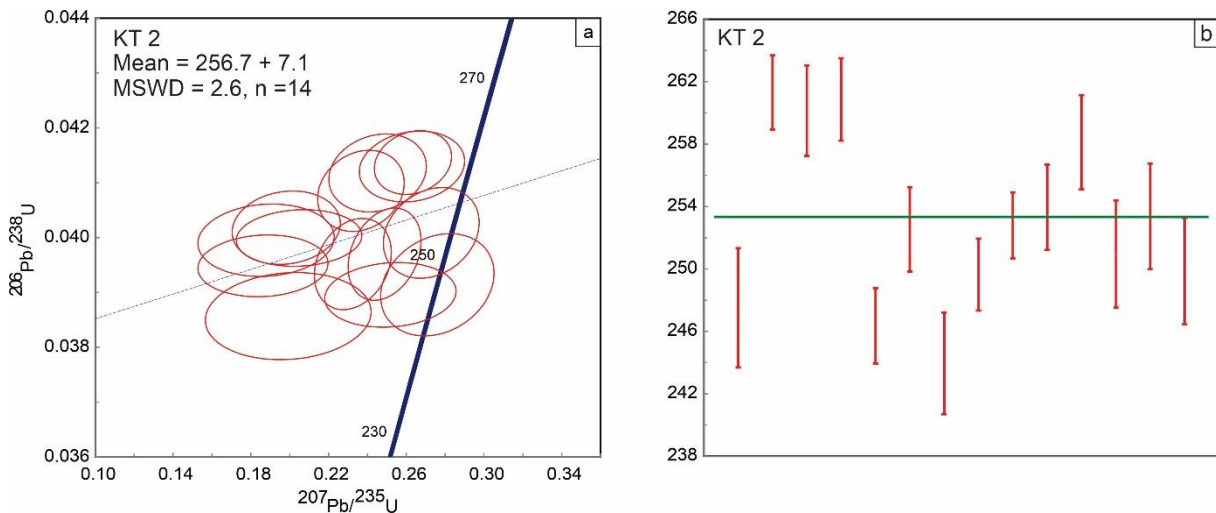


**Fig. 8.** (a) Zircon U-Pb Concordia, (b) weighted mean diagrams of the Sa Thay granite.

**Tab. 3.** LA-ICP-MS dating data of the Sa Thay granite.

| Spot  | Th/U | Isotope ratios                       |        |                                     |        |                                     |        | Age (Ma)                            |     |                                     |      |
|-------|------|--------------------------------------|--------|-------------------------------------|--------|-------------------------------------|--------|-------------------------------------|-----|-------------------------------------|------|
|       |      | <sup>207</sup> Pb/ <sup>206</sup> Pb | 1σ     | <sup>207</sup> Pb/ <sup>235</sup> U | 1σ     | <sup>206</sup> Pb/ <sup>238</sup> U | 1σ     | <sup>206</sup> Pb/ <sup>238</sup> U | 1σ  | <sup>207</sup> Pb/ <sup>235</sup> U | 1σ   |
| KT2-1 | 0.31 | 0.0527                               | 0.0033 | 0.0193                              | 0.0193 | 0.0391                              | 0.0006 | 247                                 | 3.8 | 247                                 | 15.3 |
| -2    | 0.33 | 0.0477                               | 0.0017 | 0.0131                              | 0.0131 | 0.0414                              | 0.0004 | 261                                 | 2.4 | 237                                 | 10.6 |
| -3    | 0.32 | 0.0452                               | 0.0024 | 0.0166                              | 0.0166 | 0.0412                              | 0.0005 | 260                                 | 2.9 | 223                                 | 13.5 |
| -4    | 0.35 | 0.0482                               | 0.0019 | 0.0179                              | 0.0179 | 0.0413                              | 0.0004 | 261                                 | 2.6 | 237                                 | 14.4 |
| -5    | 0.32 | 0.0495                               | 0.0021 | 0.0223                              | 0.0223 | 0.0390                              | 0.0004 | 246                                 | 2.4 | 228                                 | 18.1 |
| -6    | 0.34 | 0.0376                               | 0.0015 | 0.0232                              | 0.0232 | 0.0400                              | 0.0004 | 253                                 | 2.7 | 175                                 | 19.8 |
| -7    | 0.32 | 0.0424                               | 0.0022 | 0.0282                              | 0.0282 | 0.0386                              | 0.0005 | 244                                 | 3.3 | 185                                 | 23.9 |
| -8    | 0.33 | 0.0375                               | 0.0010 | 0.0221                              | 0.0221 | 0.0395                              | 0.0004 | 250                                 | 2.3 | 173                                 | 18.9 |
| -9    | 0.33 | 0.0405                               | 0.0012 | 0.0213                              | 0.0213 | 0.0400                              | 0.0003 | 253                                 | 2.1 | 189                                 | 18.0 |
| -10   | 0.33 | 0.0386                               | 0.0013 | 0.0184                              | 0.0184 | 0.0402                              | 0.0004 | 254                                 | 2.7 | 184                                 | 15.6 |
| -11   | 0.34 | 0.0440                               | 0.0015 | 0.0147                              | 0.0147 | 0.0409                              | 0.0005 | 258                                 | 3.0 | 216                                 | 12.1 |
| -12   | 0.34 | 0.0474                               | 0.0013 | 0.0124                              | 0.0124 | 0.0397                              | 0.0006 | 251                                 | 3.4 | 226                                 | 10.1 |
| -13   | 0.31 | 0.0507                               | 0.0024 | 0.0163                              | 0.0163 | 0.0401                              | 0.0005 | 253                                 | 3.4 | 245                                 | 13.0 |
| -14   | 0.34 | 0.0438                               | 0.0021 | 0.0131                              | 0.0131 | 0.0395                              | 0.0005 | 250                                 | 3.4 | 212                                 | 10.8 |

### 4.3. Hf isotopic composition

The Hafnium, Hf isotopic composition of individual zircon grains was determined concurrently with the U-Pb isotopic analysis (Table 4). The results indicated that the Lutetium / Hafnium (<sup>176</sup>Lu / <sup>177</sup>Hf) ratios range from 0.001552 to 0.000455. The majority of the analysis's findings were less than 0.002, with most values below 0.002, suggesting a derivation from a common mantle source. The <sup>176</sup>Hf/<sup>177</sup>Hf ratios are relatively consistent, varying between 0.282473 and 0.282252. Using a crystallization age of t=257 Ma, the calculated ε<sub>Hf</sub>(t) values range from -5.2 to 12.8, with two samples (KT2-1 and KT2-5) showing ε<sub>Hf</sub>(t) values less than -10. The negative ε<sub>Hf</sub>(t) values indicate mantle-derived magmas that were contaminated by crustal material (Fig. 9). The single-stage model ages (T<sub>DM1</sub>) range from 1108 to 1390 Ma, with an average of 1236 Ma. The two-stage model ages (T<sub>DM2</sub>) range from 1440 to 1861 Ma, with an average of 1620 Ma.

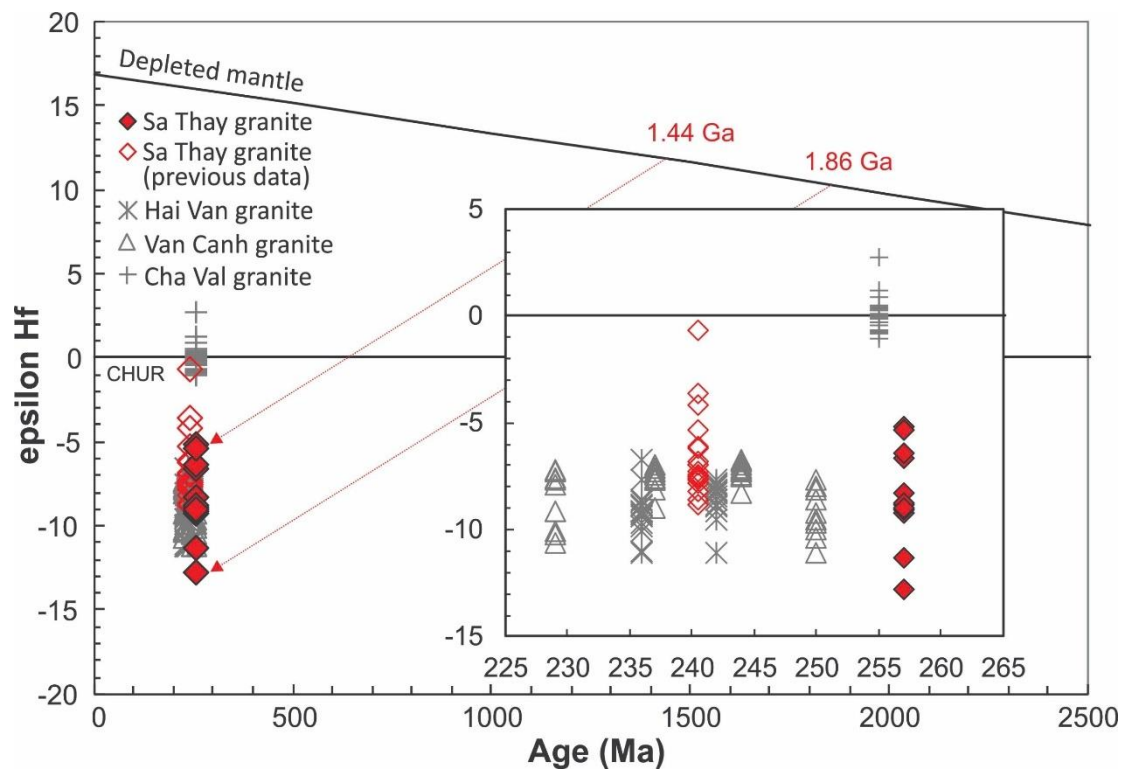


**Fig. 9.** Zircon Hf isotopic composition of Sa Thay granite.

**Tab. 4.** Zircon Hf isotopic composition of the Sa thay granite.

| Sample | $^{176}\text{Yb}/^{177}\text{Hf}$ | $^{176}\text{Lu}/^{177}\text{Hf}$ | $^{176}\text{Hf}/^{177}\text{Hf}$ | $1\sigma$ | $^{176}\text{Hf}/^{177}\text{Hf}$<br>(t) | $\epsilon\text{Hf}(t)$ | $1\sigma$ | $T_{\text{DM1}}$<br>(Ma) | $T_{\text{DM2}}$<br>(Ma) |
|--------|-----------------------------------|-----------------------------------|-----------------------------------|-----------|--|------------------------|-----------|--------------------------|--------------------------|
| KT2-1  | 0.016948                          | 0.000455                          | 0.282252                          | 0.000017  | 0.282250                                 | -12.8                  | 0.8       | 1390                     | 1861                     |
| KT2-2  | 0.038507                          | 0.001185                          | 0.282368                          | 0.000019  | 0.282362                                 | -8.9                   | 0.8       | 1255                     | 1642                     |
| KT2-3  | 0.037382                          | 0.001087                          | 0.282361                          | 0.000022  | 0.282356                                 | -9.1                   | 1.0       | 1262                     | 1655                     |
| KT2-4  | 0.042770                          | 0.001203                          | 0.282383                          | 0.000016  | 0.282377                                 | -8.3                   | 0.8       | 1234                     | 1612                     |
| KT2-5  | 0.032039                          | 0.001146                          | 0.282298                          | 0.000024  | 0.282293                                 | -11.3                  | 1.0       | 1351                     | 1777                     |
| KT2-6  | 0.031734                          | 0.000971                          | 0.282371                          | 0.000015  | 0.282366                                 | -8.7                   | 0.8       | 1244                     | 1635                     |
| KT2-7  | 0.024837                          | 0.000684                          | 0.282354                          | 0.000026  | 0.282351                                 | -9.2                   | 1.1       | 1257                     | 1664                     |
| KT2-9  | 0.050890                          | 0.001503                          | 0.282432                          | 0.000016  | 0.282425                                 | -6.6                   | 0.8       | 1174                     | 1519                     |
| KT2-10 | 0.020803                          | 0.000619                          | 0.282358                          | 0.000021  | 0.282355                                 | -9.1                   | 0.9       | 1249                     | 1655                     |
| KT2-11 | 0.045957                          | 0.001365                          | 0.282438                          | 0.000020  | 0.282432                                 | -6.4                   | 0.9       | 1161                     | 1506                     |
| KT2-12 | 0.052343                          | 0.001552                          | 0.282473                          | 0.000023  | 0.282465                                 | -5.2                   | 1.0       | 1118                     | 1440                     |
| KT2-13 | 0.030566                          | 0.000869                          | 0.282465                          | 0.000028  | 0.282461                                 | -5.3                   | 1.1       | 1108                     | 1448                     |
| KT2-14 | 0.040675                          | 0.001107                          | 0.282363                          | 0.000022  | 0.282358                                 | -9.0                   | 0.9       | 1259                     | 1651                     |

## 5. Discussion

### 5.1. Timing of magma formation

According to previously published studies, the formation age of the Sa Thay granite within the Kontum massif remains debated: (1) Based on geological field relationships and rock composition, some researchers have classified the Sa Thay granites as being of Silurian age [1], or Cretaceous age [2]; (2) U-Pb zircon dating by Vu (2014) yielded an age of 240.5 Ma. In this study, the formation age of the Sa Thay granites was determined using LA-ICP-MS U-Pb zircon isotopes. The U-Pb zircon analysis results

(summarized in Table 3) show that 5 out of 14 zircon grains lie on or close to the Concordia curve, yielding  $^{206}\text{Pb}/^{238}\text{U}$  ages around 256.7 Ma. The calculated average age is  $256.7 \pm 7.1$  Ma, corresponding to the Late Permian-Early Triassic period. This age is consistent with previously published data [5], younger than the Silurian age reported by DGMVN (1997), and older than the Cretaceous age proposed by Duyen (2006). Furthermore, the recent research by Trong (2021) determined the formation age of Sa Thay andesite to be 265 Ma, which closely aligns with the findings of this study. Therefore, the Sa Thay granite likely crystallized during a period of magmatic activity in the Permian-Triassic period.

### 5.2. Origin and geological significance of the Late Permian-Early Triassic

Sa Thay granites exhibit typical I-type granite trends based on the I-, S-, and A-type granite categorization system. The mineral assemblage of Sa Thay granite is distinguished by its abundance of anhydrous minerals, including biotite and hornblende, while aluminum-rich minerals, especially muscovite, cordierite, and garnet are entirely absent, which is typical of I-type granite. In terms of geochemical characteristics, Sa Thay granites show relatively high  $\text{SiO}_2$  and high  $\text{Al}_2\text{O}_3$  compositions, the CaO content tends to decrease gradually with increasing  $\text{SiO}_2$ , and are classified as metaluminous with A/CNK values all less than 1.1.

In terms of geochemical characteristics, the Sa Thay granites are categorized as metaluminous with low A/CNK values  $<1.1$  and exhibit comparatively high  $\text{SiO}_2$  and high  $\text{Al}_2\text{O}_3$  contents. The CaO concentration tends to gradually decrease with increasing  $\text{SiO}_2$  (Fig. 3c). Furthermore, on the  $\text{SiO}_2\text{-P}_2\text{O}_5$  and Rb-Th diagrams, the Sa Thay granite follows I-type granitic trends (Fig. 3e, f). On the chondrite- and primitive mantle-normalized diagrams (Fig. 4), the Sa Thay granite samples show depletion in Nb, Ba, Eu, Sr, and Ti and enrichment in Nd, U, and Pb, which may indicate fractional crystallization of common minerals (e.g., K-feldspar, plagioclase, biotite, and apatite). The Sa Thay granite mainly shows a fractional crystallization rather than a partial melting trend on the La vs. La/Sm diagram (Fig. 5). The Nb/Ta ratio ranges from 3.4 to 12.9, with an average of  $8.15 < 11$  [48], indicating the participation of lithospheric mantle or a subduction-modified mantle, rather than the asthenospheric mantle.

Zircon saturation [49] shows that the Sa Thay granites were formed in the temperature range of  $763^\circ\text{C}$  to  $780^\circ\text{C}$  (Table 2). The Sa Thay granites according to tectonic context by Pearce (1984) plotted in both the volcanic arc granite (VAG) and volcanic arc + syn-collision granite (VAG + syn-COLG) (Fig. 6a, b). The Hf isotopic composition of Sa Thay granites mostly has values of less than 0.002, the result showing that the Sa Thay granites were derived from melting of the same mantle source. Negative  $\varepsilon_{\text{Hf}}(t)$  values signify the involvement of partial crustal material. In addition, there are many small-grained dark xenoliths in Sa Thay granites (Fig. 2). From this, it can be assumed that Sa Thay granites were derived from mantle sources mixed with continental crustal material. According to recent research on the geology of Southeast Asia and Vietnam's territory from a plate tectonic perspective, the region was created by the assembly and collision of microcontinental plates like Sibumasu, Simao, South China, and Indochina as well as the destruction of ocean basins [5, 50-54]. Recent studies show that the Kontum massif area experienced two main thermo-tectonic stages: the early Paleozoic (Ordovician-Silurian) stage [11-15, 39, 55, 56], and the late Paleozoic-early Mesozoic (Permian-Triassic) stage [3, 18, 40, 53, 57, 58]. Researchers believe that the strong magmatic-thermal tectonic activity along suture zones like the Song Ma suture zone, the Truong Son orogenic belt, the Kon Tum massif, and the Tam Ky-Phuoc Son suture zone in Vietnam is connected to the subduction and disappearance of the Paleo-Tethys Ocean [17, 18, 38, 39, 53, 59-62]. The subduction of the Paleo-Tethys Ocean beneath the Indochina block during the Late Permian to Early Triassic periods is the so-called Indosinian Orogeny event [5]. Among these, granitoids are associated with the subduction of the Paleo-Tethys Ocean and the orogenic collision processes, characterized predominantly by the presence of I- and S-type granites [16-18, 38, 39, 59, 61, 63, 64]. In this study, the Sa Thay granites are I-type granites, with a formation age of 256.7Ma, corresponding to the Late Paleozoic period. The  $\varepsilon_{\text{Hf}}(t)$  value together with the zircon Hf model ages ( $T_{\text{DM2}}$ ) range from 1440 to 1861 Ma, indicating that the Sa Thay granites were formed by the melting and crystallization process from Paleoproterozoic ancient rocks.

In this study, the Sa Thay granite is characterized as an aluminum-saturated, I-type granite that is associated with subduction processes (Fig. 5a, b), in the context of magmatic activities related to the Andesite-type continental arc [65]. The U-Pb isotopic age (256.7Ma) of the Sa Thay granites in the Kontum massif and the I-type granites in the Northern Truong Son belt coincide with the magmatic activity spreading along the Triassic Vietnam orogenic belt [8] and concentrated along the Permian-Triassic magmatic arc (Fig. 10) [66]. Based on the geological, petrochemical, isotopic composition, and formation time characteristics described above, the Sa Thay granite is thought to have formed during the Paleo-Tethys ocean's subduction phase (290–250 Ma) beneath the Indochina block along the Song Ma suture (Fig. 10a, b).

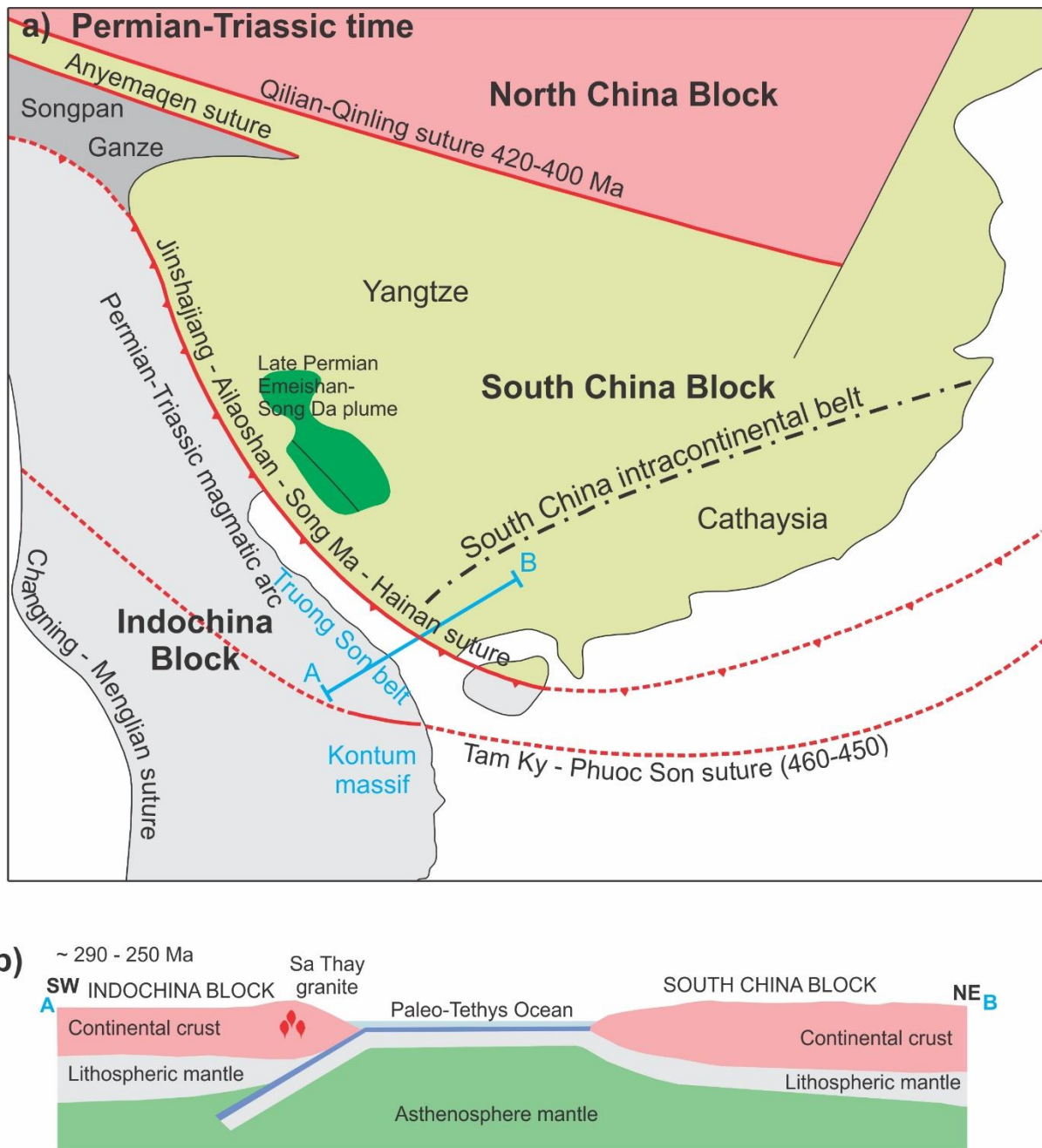


**Fig 10.** (a) Tectonic modeling of the Indochina block and its surrounding regions during the Permian and Triassic periods [66], (b) Tectonic setting for the Sa Thay granite and the other Permian-Triassic granites in Vietnam.

## 6. Conclusion

Based on the petrographic characteristics, whole rock geochemistry, U-Pb zircon age, and Hf isotopic composition in zircon of the Sa Thay granite, the following conclusions can be drawn:

Sa Thay granites in Kontum massif mainly embrace the biotite granite and hornblende biotite granite. The main mineral composition includes hornblende, biotite, plagioclase, K-feldspar, and quartz. The samples exhibit a fairly high SiO<sub>2</sub> content, medium-K content, as well as a metaluminous nature. These features are consistent with I-type granites that formed in the continental arc volcanic system.

The Lu-Hf isotope and Hf model age ( $T_{DM2}$ ), together with the presence of xenoliths and positive Pb spikes in mantle-normalized diagrams, imply that the Sa Thay granites were formed from a mantle-derived magma mixed with crustal material.

The age of the Sa Thay granite was determined by the zircon U-Pb LA-ICP-MS method, which yielded an intercept age of 256.7 Ma, (the Late Permian). Since there is a widespread distribution of I-type granites in the Truong Son belt and Kontum massif, the Sa Thay granites are believed to be associated with

the subduction of the Paleo-Tethys Ocean beneath the Indochina block during the Late Permian to Early Triassic periods (i.e. Indosinian Orogeny).

### Acknowledgments

This research is funded by Vietnam National University, Ho Chi Minh City (VNU-HCM) under grant number B2023-18-11. Authors thank the anonymous reviewers for improving the submission.

### Literature – References

1. DGMVN, Geological map and mineral resources in the Kon Tum at a scale of 1:200.000. 1997, Department of Geology and Minerals of Vietnam: Hanoi, Vietnam.
2. Duyen T.D., Geological map and mineral resources in the Kon Tum sheet at a scale of 1:50.000. 2006, Department of Geology and Minerals of Vietnam: Hanoi, Vietnam.
3. Trọng N.H., Dũng L.T., Hiếu P.T., 2021. U-Pb LA-ICP-MS zircon age in andesite of the Sa Thay area, Kontum Massif and its implication. *Vietnam Journal of Geology*, 375\_376, 1-11.
4. Dũng L.T., 2012. Examining and evaluating the capability of AuCu-Mo mineralization in Sa Thay – DakTo for planning and investment in mining in Kontum. ed. Kon Tum, Vietnam: The office of science and technology, Kon Tum, Viet Nam.
5. Tri T.V., Khuc V., 2011. Geology and earth resources of Vietnam. ed. Ha Noi, Vietnam: Publishing House for Science and Technology. 634.
6. Nam T.N., Sano Y., Terada K., Toriumi M., Van Quynh P., 2001. First SHRIMP U–Pb zircon dating of granulites from the Kontum massif (Vietnam) and tectonothermal implications. *Journal of Asian Earth Sciences*, 19(1-2), 77-84.
7. Nam T.N., Toriumi M., Sano Y., Terada K., Thang T.T., 2003. 2.9, 2.36, and 1.96 Ga zircons in orthogneiss south of the Red River shear zone in Viet Nam: evidence from SHRIMP U–Pb dating and tectonothermal implications. *Journal of Asian Earth Sciences*, 21(7), 743-753.
8. Osanai Y., Nakano N., Owada M., Nam T.N., Miyamoto T., Minh N.T., Nam N.V., Tri T.V., 2008. Collision zone metamorphism in Vietnam and adjacent South-eastern Asia: Proposition for Trans Vietnam Orogenic Belt. *Journal of Mineralogical and Petrological Sciences*, 103(4), 226-241.
9. Nakano N., Osanai Y., Owada M., Nam T.N., Charusiri P., Khamphavong K., 2013. Tectonic evolution of high-grade metamorphic terranes in central Vietnam: constraints from large-scale monazite geochronology. *Journal of Asian Earth Sciences*, 73, 520-539.
10. Jiang W., Yu J.-H., Griffin W., Pham T., Qian J., Nguyen D., 2023. Tectonic evolution of Southeast Asia documented by two periods of high-grade metamorphism in the Kon Tum Massif, Central Vietnam. *Lithos*, 454, 107277.
11. Trong N.H., Zong K., Liu Y., Yuan Y., Hieu P.T., Dũng L.T., Minh P., 2021. Early Paleozoic Arc Magmatism and Accretionary Orogenesis in the Indochina Block, Southeast Asia. *The Journal of Geology*, 129(1), 33-48.
12. Hieu P.T., Dũng N.T., Thuy N.T.B., Minh N.T., Minh P., 2016. U–Pb ages and Hf isotopic composition of zircon and bulk rock geochemistry of the Dai Loc granitoid complex in Kontum massif: Implications for early Paleozoic crustal evolution in Central Vietnam. *Journal of Mineralogical and Petrological Sciences*, 111(5), 326-336.
13. Minh N.T., Dũng N.T., Hung D.D., Minh P., Yu Y., Hieu P.T., 2020. Zircon U-Pb ages, geochemistry and isotopic characteristics of the Chu Lai granitic pluton in the Kontum massif, central Vietnam. *Mineralogy and Petrology*, 114, 289-303.
14. Jiang W., Yu J.-H., Wang X., Griffin W., Pham T., Nguyen D., Wang F., 2020. Early Paleozoic magmatism in northern Kontum Massif, Central Vietnam: Insights into tectonic evolution of the eastern Indochina Block. *Lithos*, 376, 105750.
15. Thuy N.T.B., Xuan N.T., Anh B.t., Minh P., Hieu P.T., Binh D.Q., 2025. Early Paleozoic tectonic evolution in the central Vietnam: evidence from geochronological and geochemical constraints. *International Geology Review*, 67(1), 43-59.
16. Minh P., Trung H.P., Kawaguchi K., Quynh A.N.T., Le Duc P., 2022. Geochemistry, zircon U-Pb geochronology and Sr-Nd-Hf isotopic composition of the Cha Val plutonic rocks in central Vietnam: Implications for Permian-Triassic Paleo-Tethys subduction-related magmatism. *Vietnam Journal of Earth Sciences*, 44(3), 301-326.
17. Hung D.D., Tsutsumi Y., Hieu P.T., Minh N.T., Minh P., Dũng N.T., Hung N.B., Komatsu T., Hoang N., Kawaguchi K., 2022. Van Canh Triassic granite in the Kontum Massif, central Vietnam:

- geochemistry, geochronology, and tectonic implications. *Journal of Asian Earth Sciences*: X, 7, 100075.
18. Thuy N.T.B., Hieu P.T., Xin Q., Xuan N.T., Minh P., Thu H.T., 2024. Zircon U-Pb Geochronology, Geochemistry, and Sr-Nd-Hf Isotopic Composition of Ben Giang-Que Son Complex in the Southern Truong Son Belt: Implications for Permian–Triassic Tectonic Evolution. *Minerals*, 14(6), 569.
  19. Liu Y., Zong K., Kelemen P.B., Gao S., 2008. Geochemistry and magmatic history of eclogites and ultramafic rocks from the Chinese continental scientific drill hole: subduction and ultrahigh-pressure metamorphism of lower crustal cumulates. *Chemical Geology*, 247(1-2), 133-153.
  20. Liu Y., Hu Z., Gao S., Günther D., Xu J., Gao C., Chen H., 2008. In situ analysis of major and trace elements of anhydrous minerals by LA-ICP-MS without applying an internal standard. *Chemical Geology*, 257(1-2), 34-43.
  21. Liu Y., Gao S., Hu Z., Gao C., Zong K., Wang D., 2010. Continental and oceanic crust recycling-induced melt–peridotite interactions in the Trans-North China Orogen: U–Pb dating, Hf isotopes and trace elements in zircons from mantle xenoliths. *Journal of petrology*, 51(1-2), 537-571.
  22. Liu Y., Hu Z., Zong K., Gao C., Gao S., Xu J., Chen H., 2010. Reappraisal and refinement of zircon U-Pb isotope and trace element analyses by LA-ICP-MS. *Chinese Science Bulletin*, 55, 1535-1546.
  23. Wiedenbeck M., Alle P., Corfu F., Griffin W., Meier M., Oberli F.v., Quadt A.v., Roddick J., Spiegel W., 1995. Three natural zircon standards for U-Th-Pb, Lu-Hf, trace element and REE analyses. *Geostandards newsletter*, 19(1), 1-23.
  24. Ludwig K., 2003. User's manual for isoplot 3.00, a geochronological toolkit for microsoft excel. Berkeley Geochronology Center, Special Publication, 4, 25-32.
  25. Hu Z., Liu Y., Gao S., Xiao S., Zhao L., Günther D., Li M., Zhang W., Zong K., 2012. A “wire” signal smoothing device for laser ablation inductively coupled plasma mass spectrometry analysis. *Spectrochimica Acta Part B: Atomic Spectroscopy*, 78, 50-57.
  26. Hu Z., Liu Y., Gao S., Hu S., Dietiker R., Günther D., 2008. A local aerosol extraction strategy for the determination of the aerosol composition in laser ablation inductively coupled plasma mass spectrometry. *Journal of Analytical Atomic Spectrometry*, 23(9), 1192-1203.
  27. Hu Z., Liu Y., Gao S., Liu W., Zhang W., Tong X., Lin L., Zong K., Li M., Chen H., 2012. Improved in situ Hf isotope ratio analysis of zircon using newly designed X skimmer cone and jet sample cone in combination with the addition of nitrogen by laser ablation multiple collector ICP-MS. *Journal of Analytical Atomic Spectrometry*, 27(9), 1391-1399.
  28. Söderlund U., Patchett P.J., Vervoort J.D., Isachsen C.E., 2004. The  $^{176}\text{Lu}$  decay constant determined by Lu–Hf and U–Pb isotope systematics of Precambrian mafic intrusions. *Earth and Planetary Science Letters*, 219(3-4), 311-324.
  29. Blichert-Toft J., Albarède F., 1997. The Lu-Hf isotope geochemistry of chondrites and the evolution of the mantle-crust system. *Earth and Planetary Science Letters*, 148(1-2), 243-258.
  30. Griffin W., Pearson N., Belousova E., Jackson S.v., Van Acherterbergh E., O'Reilly S.Y., Shee S., 2000. The Hf isotope composition of cratonic mantle: LAM-MC-ICPMS analysis of zircon megacrysts in kimberlites. *Geochimica et cosmochimica acta*, 64(1), 133-147.
  31. Griffin W., Wang X., Jackson S., Pearson N., O'Reilly S.Y., Xu X., Zhou X., 2002. Zircon chemistry and magma mixing, SE China: in-situ analysis of Hf isotopes, Tonglu and Pingtan igneous complexes. *Lithos*, 61(3-4), 237-269.
  32. Whalen J.B., Currie K.L., Chappell B.W., 1987. A-type granites: geochemical characteristics, discrimination and petrogenesis. *Contributions to Mineralogy and Petrology*, 95(4), 407-419.
  33. Middlemost E.A., 1994. Naming materials in the magma/igneous rock system. *Earth-Science Reviews*, 37(3-4), 215-224.
  34. Peccerillo A., Taylor S., 1976. Geochemistry of eocene calc-alkaline volcanic rocks from the Kastamonu area, Northern Turkey. *Contributions to Mineralogy and Petrology*, 58, 63–81.
  35. Maniar P.D., Piccoli P.M., 1989. Tectonic discrimination of granitoids. *Geological society of America bulletin*, 101(5), 635-643.
  36. Chappell B., 1999. Aluminium saturation in I-and S-type granites and the characterization of fractionated haplogranites. *Lithos*, 46(3), 535-551.
  37. Vu T.H., Indosinian tectonic and magmatic evolution of the PoKo suture in the Western Highlands, Central Vietnam. 2014, China University of Geosciences: Beijing.
  38. Hoang N.K., Anh N.T.Q., Minh P., Hieu P.T., Thao N.T., 2023. Geochemistry and zircon U-Pb geochronology of the Dak Krong plutonic rocks in the Kontum Massif (central Vietnam) and their petrogenetic implications. *Vietnam Journal of Earth Sciences*.

39. Shi M.-F., Lin F.-C., Fan W.-Y., Deng Q., Cong F., Tran M.-D., Zhu H.-P., Wang H., 2015. Zircon U–Pb ages and geochemistry of granitoids in the Truong Son terrane, Vietnam: Tectonic and metallogenic implications. *Journal of Asian Earth Sciences*, 101, 101-120.
40. Hieu P.T., Yang Y.-Z., Binh D.Q., Nguyen T.B.T., Dung L.T., Chen F., 2015. Late Permian to Early Triassic crustal evolution of the Kontum massif, central Vietnam: zircon U–Pb ages and geochemical and Nd–Hf isotopic composition of the Hai Van granitoid complex. *International Geology Review*, 57(15), 1877-1888.
41. Sun S.S., McDonough W.F., 1989. Chemical and isotopic systematics of oceanic basalts: implications for mantle composition and processes. Geological Society, London, Special Publications, 42(1), 313-345.
42. Li J.-X., Qin K.-Z., Li G.-M., Xiao B., Chen L., Zhao J.-X., 2011. Post-collisional ore-bearing adakitic porphyries from Gangdese porphyry copper belt, southern Tibet: melting of thickened juvenile arc lower crust. *Lithos*, 126(3-4), 265-277.
43. Pearce J.A., Harris N.B., Tindle A.G., 1984. Trace element discrimination diagrams for the tectonic interpretation of granitic rocks. *Journal of Petrology*, 25(4), 956-983.
44. Corfu F., Hanchar J.M., Hoskin P.W., Kinny P., 2003. Atlas of zircon textures. *Reviews in mineralogy and geochemistry*, 53(1), 469-500.
45. Hoskin P.W., Schaltegger U., 2003. The composition of zircon and igneous and metamorphic petrogenesis. *Reviews in Mineralogy and Geochemistry*, 53(1), 27-62.
46. Pearce J.A., Peate D.W., 1995. Tectonic implications of the composition of volcanic arc magmas. *Annual Review Of Earth And Planetary Sciences*, 23, 251-286.
47. Plank T., Langmuir C.H., 1998. The chemical composition of subducting sediment and its consequences for the crust and mantle. *Chemical geology*, 145(3-4), 325-394.
48. Green T.H., 1995. Significance of Nb/Ta as an indicator of geochemical processes in the crust-mantle system. *Chemical geology*, 120(3-4), 347-359.
49. Watson E.B., Harrison T.M., 1983. Zircon saturation revisited: temperature and composition effects in a variety of crustal magma types. *Earth and Planetary Science Letters*, 64(2), 295-304.
50. Metcalfe I., 2005. Asia: south-east. *Encyclopedia of geology*, 1, 169-198.
51. Metcalfe I., 2011. Tectonic framework and Phanerozoic evolution of Sundaland. *Gondwana Research*, 19(1), 3-21.
52. Metcalfe I., 2013. Gondwana dispersion and Asian accretion: Tectonic and palaeogeographic evolution of eastern Tethys. *Journal of Asian Earth Sciences*, 66, 1-33.
53. Tran H.T., Zaw K., Halpin J.A., Manaka T., Meffre S., Lai C.-K., Lee Y., Le H.V., Dinh S., 2014. The Tam Ky-Phuoc Son Shear Zone in central Vietnam: Tectonic and metallogenic implications. *Gondwana Research*, 26(1), 144-164.
54. Halpin J.A., Tran H.T., Lai C.-K., Meffre S., Crawford A.J., Zaw K., 2016. U–Pb zircon geochronology and geochemistry from NE Vietnam: A ‘tectonically disputed’ territory between the Indochina and South China blocks. *Gondwana Research*, 34, 254-273.
55. Gardiner N.J., Hickman A.H., Kirkland C.L., Lu Y., Johnson T., Zhao J.-X., 2017. Processes of crust formation in the early Earth imaged through Hf isotopes from the East Pilbara Terrane. *Precambrian Research*, 297, 56-76.
56. Dung N.T., Anh T.T., Hieu P.T., Minh P., Truong L.X., Minh N.T., Hung D.D., 2024. Crustal evolution of Paleozoic-Mesozoic granitoid in Dakrong–A Luoi area, Truong Son belt, central Vietnam: evidence from zircon U–Pb geochronology, geochemistry, and Hf isotope composition. *International Geology Review*, 1-25.
57. Owada M., Osanai Y., Nakano N., Adachi T., Kitano I., Tri T.V., Kagami H., 2016. Late Permian plume–related magmatism and tectonothermal events in the Kontum Massif, central Vietnam. *Journal of Mineralogical and Petrological Sciences*, 111(3), 181-195.
58. Nakano N., Osanai Y., Owada M., Binh P., Hokada T., Kaiden H., Bui V.T., 2021. Evolution of the Indochina Block from its formation to amalgamation with Asia: Constraints from protoliths in the Kontum Massif, Vietnam. *Gondwana Research*, 90, 47-62.
59. Carter A., Roques D., Bristow C., Kinny P., 2001. Understanding Mesozoic accretion in Southeast Asia: Significance of Triassic thermotectonism (Indosinian orogeny) in Vietnam. *Geology*, 29(3), 211-214.
60. Hoa T.T., Anh T.T., Phuong N.T., Dung P.T., Anh T.V., Izokh A.E., Borisenko A.S., Lan C.Y., Chung S.L., Lo C.H., 2008. Permo-Triassic intermediate–felsic magmatism of the Truong Son belt, eastern margin of Indochina. *Comptes Rendus Geoscience*, 340(2-3), 112-126.

61. Wang S., Mo Y., Wang C., Ye P., 2016. Paleotethyan evolution of the Indochina Block as deduced from granites in northern Laos. *Gondwana Research*, 38, 183-196.
62. Thanh T.V., Hieu P.T., Minh P., Nhuan D.V., Thuy N.T.B., 2019. Late Permian-Triassic granitic rocks of Vietnam: the Muong Lat example. *International Geology Review*, 61(15), 1823-1841.
63. Hieu P.T., Li S.-Q., Yu Y., Thanh N.X., Dung L.T., Tu V.L., Siebel W., Chen F., 2017. Stages of late Paleozoic to early Mesozoic magmatism in the Song Ma belt, NW Vietnam: evidence from zircon U-Pb geochronology and Hf isotope composition. *International Journal of Earth Sciences*, 106(3), 855-874.
64. Hieu P.T., Anh N.T.Q., Minh P., Thuy N.T.B., 2020. Geochemistry, zircon U-PB ages and HF isotopes of the Muong Luan granitoid pluton, Northwest Vietnam and its petrogenetic significance. *Island Arc*, 29(1), e12330.
65. Barbarin B., 1999. A review of the relationships between granitoid types, their origins and their geodynamic environments. *Lithos*, 46(3), 605-626.
66. Faure M., Nguyen V.V., Hoai L.T.T., Lepvrier C., 2018. Early Paleozoic or Early-Middle Triassic collision between the South China and Indochina Blocks: The controversy resolved? Structural insights from the Kon Tum massif (Central Vietnam). *Journal of Asian Earth Sciences*, 166, 162-180.